

## Diffusional Coupling between Micro and Macroporosity for NMR Relaxation in Sandstones and Grainstones<sup>1</sup>

Vivek Anand<sup>2</sup> and George J. Hirasaki<sup>3</sup>

### ABSTRACT

The interpretation of NMR measurements with fluid saturated rocks assumes that the  $T_1$  or  $T_2$  distribution is directly related to the pore size distribution. In many cases, this assumption is valid. However, the assumption breaks down if the fluid in different sized pores is coupled through diffusion. In such cases, the estimation of formation properties such as permeability and irreducible water saturation using the traditional  $T_{2,cutoff}$  method gives erroneous results. Several techniques like “spectral” BVI and tapered  $T_{2,cutoff}$  were introduced to take into account the effects of diffusional coupling for better estimation of properties.

This paper aims to provide a theoretical and experimental understanding of NMR relaxation in systems with diffusional coupled micro and macropores. Relaxation is modeled such that the fluid molecules relax at the surface of the micropore and simultaneously diffuse between the two pore types. The  $T_2$  distribution of the pore is a function of several parameters including micropore surface relaxivity, fluid diffusivity and pore geometry. The governing parameters are combined in a single coupling parameter ( $\alpha$ ) that is defined as the ratio of the characteristic relaxation rate of the coupled pore to the rate of diffusional mixing of magnetization between micro and macropore. Depending on the value of  $\alpha$ , the two pore types can communicate through total coupling, intermediate coupling or decoupled regimes.

The model is applied to treat diffusional coupling in sandstones with a distribution of macropores lined with clay flakes. Simulations are verified by comparing with experimental results for chlorite-coated, North Burbank sandstone. It is observed that the relaxation time distribution shows a bimodal distribution at 100% water saturation but a unimodal distribution when saturated with hexane. This occurs because the extent of coupling is higher for hexane than for water due to lower relaxivity and higher diffusivity of hexane. The  $\alpha$  values indicate intermediate coupling for water and strong coupling for hexane.

The model is also applied to explain pore coupling in grainstone carbonates with intra and intergranular porosity. In this case,  $\alpha$  is shown to have a quadratic dependence on grain radius and inverse dependence on micropore radius. The theory is experimentally validated on several systems with microporous particles of varying grain diameters and known microporosities. Here too, the  $T_2$  distribution at 100% water saturation varies from bimodal for coarse-grained particles to unimodal for fine-grained particles. The transition from bimodal to unimodal distribution is also predicted theoretically from the values of  $\alpha$ .

**Keywords:** NMR, diffusional coupling, microporosity, relaxation time cutoffs

Manuscript received by the Editor September 26, 2005; revised manuscript received June 18, 2007.

<sup>1</sup>Paper originally presented at the SPWLA 46th Annual Logging Symposium, New Orleans, Louisiana USA, June 26-29, 2005, paper KKK

<sup>2</sup>Schlumberger Oilfield Services, Sugar Land, TX, USA; E-mail: vanand@slb.com

<sup>3</sup>Rice University, Houston, TX, USA; E-mail: gjh@rice.edu

©2007 Society of Petrophysicists and Well Log Analysts. All rights reserved.

## INTRODUCTION

NMR  $T_2$  measurements are often used to estimate the pore structure and formation properties such as porosity, permeability and irreducible water saturation. NMR estimation of pore size distribution assumes that in the fast diffusion limit,  $T_2$  of a fluid in a single pore is given as

$$\frac{1}{T_2} = \frac{1}{T_{2B}} + \rho_2 \left( \frac{S}{V} \right)_{pore} \quad (1)$$

where  $T_{2B}$  is the bulk relaxation time,  $\rho_2$  is the transverse surface relaxivity and  $(S/V)_{pore}$  is the pore surface-to-volume ratio. For a rock sample having a pore size distribution, each pore size is assumed to be associated with a  $T_2$  component and the net magnetization relaxes as a multi-exponential decay.

$$M(t) = \sum_j f_j \exp\left(-\frac{t}{T_{2,j}}\right) \quad (2)$$

where  $f_j$  is the amplitude of each  $T_{2,j}$ . Such interpretation of NMR measurements assumes that pores of different sizes relax independent of each other. In many cases, this assumption is valid. However, it is observed that the assumption often fails for shaly sandstones and carbonates especially in grainstones and packstones. Ramakrishnan et al. (1999) explained that the failure could be understood by considering the diffusion of magnetization between intra (micro) and intergranular (macro) pores. The resulting  $T_2$  distribution is influenced by surface-to-volume ratio of both micro- and macropores and thus, the correspondence between  $T_2$  and pore size distribution is lost. In such cases, traditional method of employing a sharp  $T_{2,cutoff}$  for estimating bound fluid fractions and permeability would not be applicable.

The effect of diffusional coupling on accurate estimation of irreducible saturation is illustrated for the case of clay

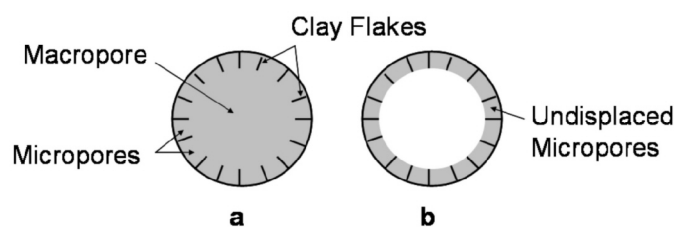


**FIG. 1** Conceptual model of pore coupling in clay lined pore in sandstones (Straley et al., 1995). (a) 100% water saturated pore. Fluid in micropores relaxes with  $T_2 > T_{2,cutoff}$  due to diffusional exchange with the macropore. (b) Pore at irreducible water saturation. Fluid relaxes with a rate proportional to surface to volume ratio of the micropore.

lined pores in sandstones. Figure 1 shows the schematic diagram of a clay lined pore (Straley et al., 1995) (a) at 100% water saturation and (b) at irreducible saturation after capillary drainage of the macropore. First consider the case of the pore at irreducible saturation in Figure 1(b). Since the macropore is drained, there is no diffusional exchange between fluid in micro- and macropore. Thus, the fluid in micropores relaxes with a rate proportional to the surface-to-volume ratio of the micropores. Now consider the case of 100% water-saturated pore in Figure 1(a). If the fluid in micropores is in diffusional exchange with that in the macropore, its apparent volume is larger even though the surface area for relaxation remains same. Thus, the fluid in micropores relaxes with a longer relaxation time than at irreducible saturation. If a sharp  $T_{2,cutoff}$  based on the relaxation time of micropores at irreducible saturation is employed, it may underpredict the irreducible saturation because a fraction of fluid in micropores is relaxing slower than  $T_{2,cutoff}$ . Techniques like “spectral” BVI and tapered  $T_{2,cutoff}$  (Coates et al., 1998; Kleinberg et al., 1997) usually provide better estimates in such cases by assuming an irreducible fraction which is diffusively coupled with bulk pore fluid for each pore size. However, a theoretical basis for the application of these techniques needs to be established.

## DIFFUSIONAL COUPLING BETWEEN MICRO AND MACROPORES

### Mathematical modeling

We begin by numerically simulating the decay of magnetization in the symmetry element between two clay flakes in the pore model of Figure 1. Figure 2 shows the simplified

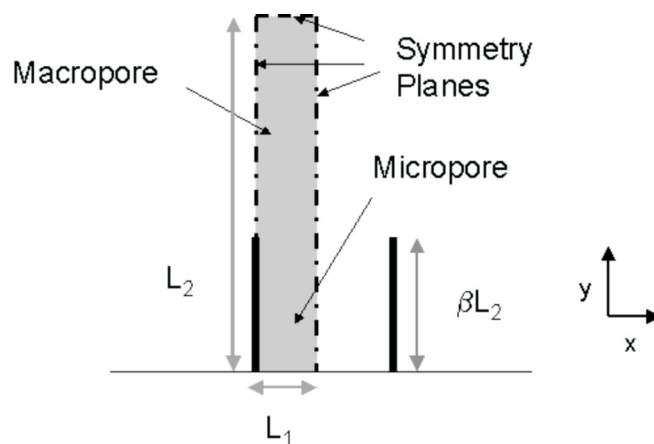


**FIG. 2** Physical model of coupled pore geometry. Fluid molecules relax at the micropore surface while diffusing between the micro and macropore.

pore model consisting of a clay-bounded micropore adjacent to a macropore. The curvature of the outer grain surface and the thickness of the clay flake are neglected. The fluid molecules relax at the surface of the micropore and simultaneously diffuse between the two pore types. As a result, the  $T_2$  distribution of the pore is determined by several parameters such as micropore surface relaxivity, diffusivity of the fluid and geometry of the pore system. The simple model helps to keep the analysis tractable and also captures the essential features of more complicated pore coupling models (Toumelin et al., 2003).

The coupled pore is defined by three geometrical parameters: half length to the middle of macropore ( $L_2$ ), half-distance between clay flakes ( $L_1$ ) and microporosity fraction ( $\beta$ ). The decay of magnetization per unit volume ( $M$ ) in the pore is given by the Bloch-Torrey equation

$$\frac{\partial M}{\partial t} = D\nabla^2 M - \frac{M}{T_{2,B}} \quad (3)$$

where  $D$  is the diffusivity of the fluid. The boundary conditions are

$$D\vec{n} \cdot \nabla M + \rho M = 0 \text{ at micropore surface} \quad (4)$$

$$\vec{n} \cdot \nabla M = 0 \text{ at symmetry planes} \quad (5)$$

where  $\vec{n}$  is the unit normal pointing outwards from the pore surface and  $\rho$  is the surface relaxivity. A uniform magnetization is assumed in the entire pore initially. In addition, the bulk relaxation rate is assumed to be very small in comparison to surface relaxation and is neglected.

We introduce characteristic parameters to make the governing equations (3-5) dimensionless. Expressing the equations in dimensionless form helps to characterize the systems with fewer parameters. The spatial variables are, thus, normalized with respect to the half-length of the pore ( $L_2$ ), magnetization with respect to initial magnetization and time with respect to a characteristic relaxation time,  $T_{2,c}$  defined as

$$T_{2,c} = \frac{V_{total}}{\rho S_{active}} = \frac{L_1 L_2}{\rho \beta L_2} = \frac{L_1}{\rho \beta} \quad (6)$$

In the above equation,  $S_{active}$  refers to the surface of the micropore at which relaxation is taking place and  $V_{total}$  refers to the total volume of the pore. An analogous relaxation time of the micropore,  $T_{2,\mu}$ , is defined as

$$T_{2,\mu} = \frac{1}{\rho} \left( \frac{V}{S} \right)_\mu = \frac{\beta L_2 L_1}{\rho \beta L_2} = \frac{L_1}{\rho} \quad (7)$$

where  $(V/S)_\mu$  refers to volume-to-surface ratio of the

micropore. The characteristic relaxation time  $T_{2,c}$  is related to  $T_{2,\mu}$  by comparing equations (6) and (7)

$$\Rightarrow T_{2,c} = \frac{T_{2,\mu}}{\beta} \quad (8)$$

We also introduce two dimensionless groups, namely the aspect ratio of the pore  $\eta$  and Brownstein number  $\mu$  (Brownstein and Tarr, 1979), defined as

$$\eta = \frac{L_2}{L_1} \quad (9)$$

$$\mu = \frac{\rho L_2}{D} \quad (10)$$

The dimensionless groups can be combined into a single parameter called coupling parameter ( $\alpha$ ) defined as

$$\alpha = \beta \eta \mu = \frac{\rho \beta L_2^2}{D L_1} \quad (11)$$

$\eta$  is the aspect ratio of the characteristic dimension of the macropore to that of the micropore.  $\mu$  and  $\alpha$  are ratios of the relaxation rate to the diffusion rate but  $\mu$  treats the system as a single macropore while  $\alpha$  includes the contribution of the micropore to the total surface-to-volume ratio. The physical significance of the parameters is detailed in the Results section. The governing equations can thus be expressed in terms of above mentioned dimensionless parameters as given in Appendix A. A finite difference Alternating Direction Implicit technique (Peaceman and Rachford, 1955) is employed for the numerical solution of the dimensionless equations. The details of the numerical technique are described in Appendix B.

## Results

The decay of magnetization in the coupled pore is characterized by three parameters; aspect ratio of the pore ( $\eta$ ), microporosity fraction ( $\beta$ ) and Brownstein number ( $\mu$ ). Depending on the value of  $\mu$ , defined as,

$$\mu = \frac{\text{Relaxation rate}}{\text{Diffusion rate}} = \frac{\rho / L_2}{D / L_2^2} = \frac{\rho L_2}{D} \quad (12)$$

the decay can be classified into fast, intermediate and slow diffusion regimes. In the fast diffusion regime ( $\mu \ll 1$ ), the lowest eigen value of equation (3) completely dominates and the decay curve is mono-exponential. In the slow diffusion regime ( $\mu \gg 10$ ), the higher modes also contribute to the relaxation and the decay curve is multi-exponential (Brownstein and Tarr, 1979). These diffusion regimes are

visualized with the help of snapshots of magnetization in the pore at intermediate decay times. Figure 3 shows the contour plots of magnetization for  $\beta = 0.5$  and  $\eta = 10$  at dimensionless time  $t = 1$  for various values of  $\mu$ . For  $\mu$  small compared to 1 ( $\mu = 0.1$ ), fast diffusion leads to nearly homogenous magnetization in the entire pore. With the increase in the value of  $\mu$ , gradients in magnetization along the longitudinal direction become substantial. These gradients imply that the micropore is relaxing much faster than the macropore.

Note that  $\mu$  is based on an analysis for a one-dimensional system with a single characteristic length ( $L_2$ ). For a one dimensional pore,  $\mu$  can also be expressed as the square of the ratio of the pore length to the diffusion length as shown

$$\mu = \frac{\rho L_2}{D} = \frac{L_2^2}{DL_2/\rho} = \left( \frac{L_2}{\sqrt{DT_{2,1-D}}} \right)^2. \quad (13)$$

Here  $1/T_{2,1-D}$  is the relaxation rate of the one-dimensional pore given as

$$\frac{1}{T_{2,1-D}} = \rho \left( \frac{S}{V} \right)_{pore} = \frac{\rho}{L_2}. \quad (14)$$

The assumption of a single surface-to-volume ratio inherent in the definition of  $\mu$  fails for a system of coupled micro and macropore with different surface-to-volume ratios. Figure 4 shows the contour plots of magnetization at dimensionless time  $t = 1$  for three systems with  $\beta = 0.5$  and  $\mu = 0.1$  but with increasing aspect ratios. Even though  $\mu$  remains same, the

systems with larger  $\eta$  show larger gradients in magnetization. This increase in gradients is because as  $\eta$  increases, the dimension of micropore decreases ( $\eta = L_2/L_1$ ) and thus, the relaxation rate of micropore increases. Since  $\mu$  is independent of the micropore dimension, it can not characterize relaxation regimes in coupled pore systems.

### Coupling parameter

Two processes characterize the decay of magnetization in the coupled geometry: relaxation of spins at the micropore surface and diffusion of spins between the micro- and macropores. If the relaxation of spins in the micropore is much faster than the inter-pore diffusion, coupling between the two pore types is small. On the other hand, if the diffusion rate is much greater than the relaxation rate, the two pores are significantly coupled with each other. Thus, the extent of coupling is characterized with the help of a coupling parameter ( $\alpha$ ) that compares the characteristic relaxation rate of the pore (equation (6)) to the rate of diffusional mixing of spins between the micro and macropore, i.e.

$$\alpha = \frac{1/T_{2,c}}{D/L_2^2} = \frac{\rho\beta/L_1}{D/L_2^2} = \frac{\rho\beta L_2^2}{DL_1}. \quad (15)$$

The physical significance of  $\alpha$  is illustrated with the help of simulated  $T_2$  distributions for the previously mentioned case of  $\beta = 0.5$  and  $\eta = 10$  as shown in Figure 5. For small  $\alpha$  ( $= 0.5$ ), relaxation at the micropore surface is small compared to diffusional mixing between the two pore types.

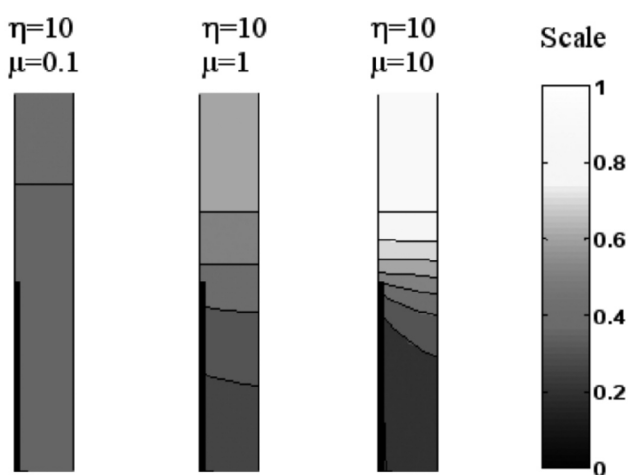


**FIG. 3** Contour plots of magnetization at  $t = 1$  in coupled pores with  $\beta = 0.5$  and  $\eta = 10$  and different values of  $\mu$ . The gradients along the longitudinal direction for larger  $\mu$  imply that micropore is relaxing faster compared to macropore.

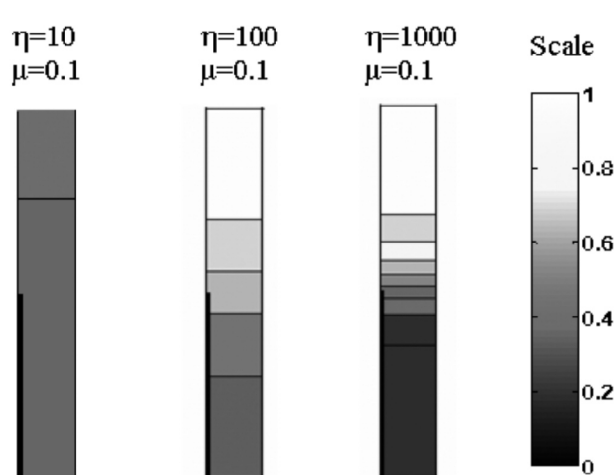


**FIG. 4** Contour plots of magnetization at  $t = 1$  in coupled pores with  $\beta = 0.5$  and  $\mu = 0.1$  and different values of  $\eta$ . For comparison, the aspect ratios are not drawn to scale. Note the difference in contour plots for systems with same  $\mu$ .

Thus, the micro and macropore relax at the same rate and the  $T_2$  distribution shows a single peak. As the value of  $\alpha$  increases ( $\alpha = 5$ ), some spins in the micropore are able to relax faster than they can diffuse into the macropore. This results in the appearance of a peak at short relaxation times (micropore peak). In addition, the spins in the macropore diffuse to the micropore slowly and thus, the macropore peak shifts towards longer relaxation times. As a still weaker coupling regime is approached ( $\alpha = 50$ ), inter-pore diffusion becomes negligible and the entire micropore relaxes independent of the macropore.

$\alpha$  can also be expressed as the square of the ratio of the length of the pore to the diffusion length in characteristic relaxation time  $T_{2,c}$  (equation (6)), as shown below

$$\alpha = \frac{\rho\beta L_2^2}{DL_1} = \frac{L_2^2}{D(L_1/\rho\beta)} = \left(\frac{L_2}{\sqrt{DT_{2,c}}}\right)^2. \quad (16)$$

If the macropore length is much larger than the diffusion distance in characteristic time, i.e.  $L_2 \gg \sqrt{DT_{2,c}} \Rightarrow \alpha \gg 1$ , the

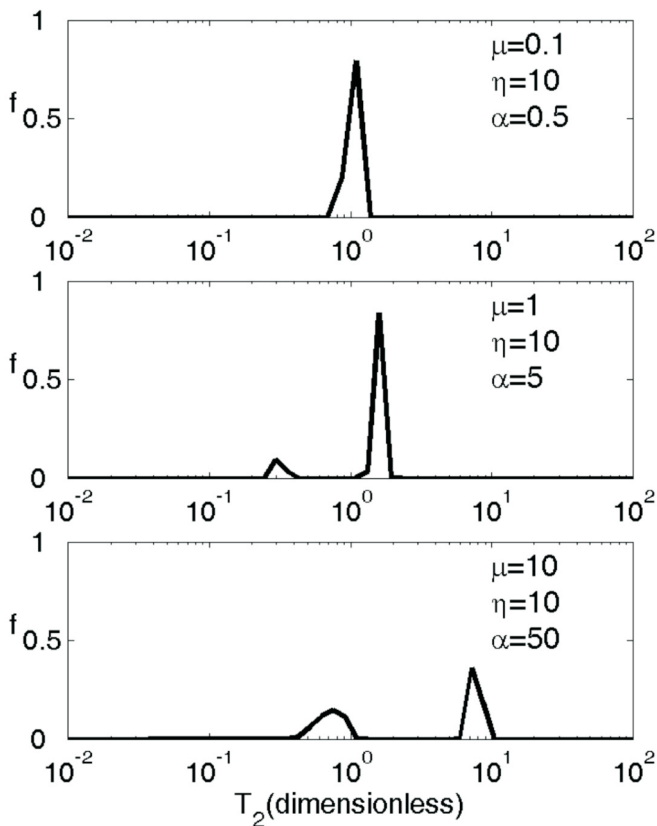


FIG. 5 Simulated  $T_2$  distributions of coupled pores with  $\beta = 0.5$  and  $\eta = 10$  and different values of  $\mu$ . The systems transition from unimodal to bimodal distribution with increase in  $\alpha$ .

pores are decoupled and vice versa. Since the characteristic relaxation time takes into account the effective surface-to-volume ratio of the coupled pore,  $\alpha$  provides a better metric than  $\mu$  to quantify coupling between micro and macropore. Figure 6 shows the simulated  $T_2$  distributions of systems with  $\beta = 0.5$  and  $\mu = 0.1$  but with increasing  $\eta$ . The systems progressively transition from unimodal to bimodal distribution as  $\eta$  increases even though  $\mu$  remains same. The decrease in coupling is however, quantified by increasing values of  $\alpha$ .

The relaxation characteristics of micro- and macropores, as demonstrated in  $T_2$  distributions of Figures 5 and 6, are separately analyzed in terms of  $\alpha$  as described below.

**Micro pore relaxation**

The fraction of total area under the micropore peak,  $\psi$ , in the  $T_2$  distribution gives the magnitude of the fraction of the microporosity which is decoupled from the rest of the pore. Thus,  $\psi$  serves as the criterion to quantify the extent of coupling between micro- and macropores. For totally coupled

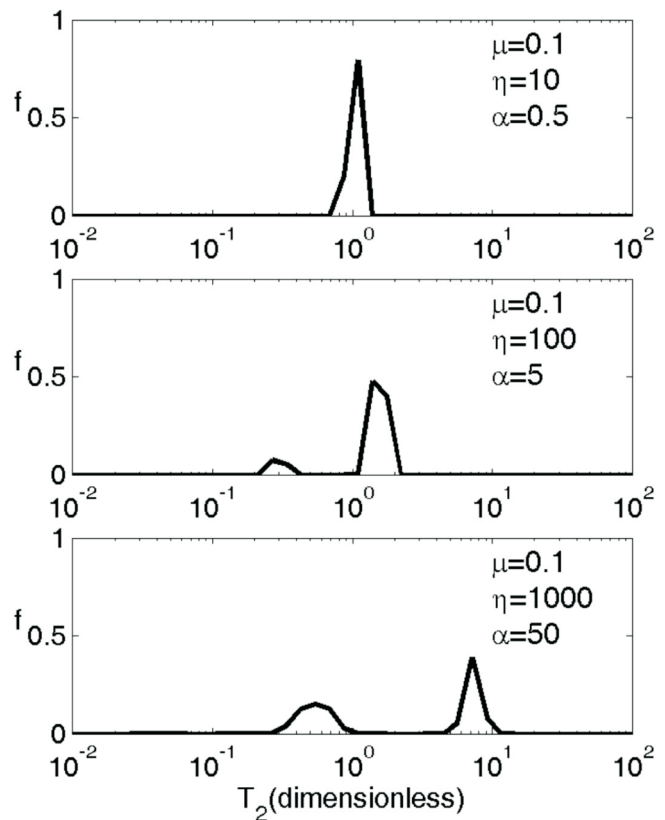


FIG. 6 Simulated  $T_2$  distributions of coupled pores with  $\beta = 0.5$  and  $\mu = 0.1$  and different values of  $\eta$ . The systems transition from unimodal to bimodal distribution with increase in  $\alpha$  even though  $\mu$  remains same.

micro and macropore  $\psi = 0$  while for decoupled pores  $\psi = \beta$ . A value of  $\psi$  between 0 and  $\beta$  indicates intermediate state of diffusional coupling. Figure 7 shows the plot of  $\psi$  normalized by  $\beta$  (henceforth referred to as independent microporosity fraction) with  $\alpha$ . The curves correspond to different  $\beta$  and span a range of  $\eta$  from 10 to 1000. The results show that depending on the value of  $\alpha$ , the micro and macropore can be in one of the three states of:

1. Total coupling ( $\alpha < 1$ ): For values of  $\alpha$  less than 1, diffusion is much faster than the relaxation of the magnetization in the micropore. Thus, the micropore is totally coupled with the macropore and the entire pore relaxes with a single relaxation rate.
2. Intermediate coupling ( $1 < \alpha < 250$ ): In this case, diffusion is just fast enough to couple part of the micropore with the macropore. The  $T_2$  distribution consists of distinct peaks for the two pore types but the amplitudes of the peaks are not proportional to the porosity fractions.
3. Decoupled ( $\alpha > 250$ ): The two pore types relax independent of each other and the  $T_2$  spectrum consists of separate peaks with amplitudes representative of the porosity fractions ( $\beta$  and  $1-\beta$  for micro and macroporosity, respectively). Further, the dimensionless relaxation time of the micropore peak reaches a value  $\beta$  (Appendix C) indicating complete independence of the two pores.

The independent microporosity fraction correlates more strongly with  $\alpha$  than with  $\mu$  (inset in Figure 7). This is because  $\alpha$  has dependence on the length scale of both micro and macropore and thus, provides a better measure to quantify the extent of coupling.

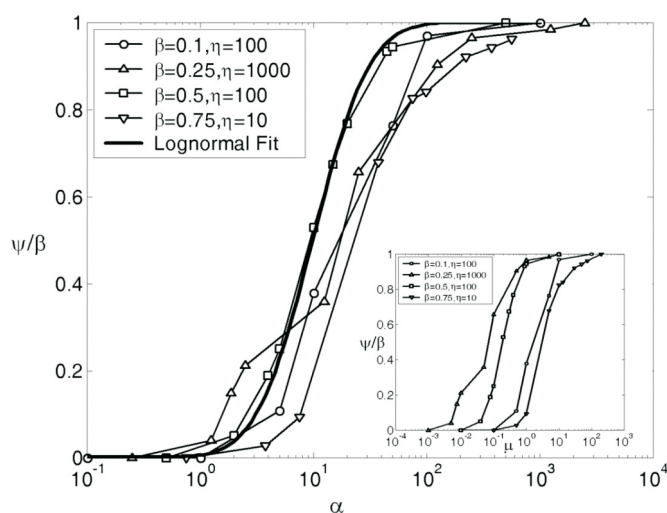


FIG. 7 Independent microporosity fraction ( $\psi/\beta$ ) shows lognormal relationship with  $\alpha$ . The inset shows plot of ( $\psi/\beta$ ) with  $\mu$ .

The sigmoidal character of the curves in Figure 7 suggests that we can establish a lognormal relationship between the independent microporosity fraction and  $\alpha$ . Mathematically, the relationship can be expressed as

$$\frac{\psi}{\beta} = \frac{1}{2} \left[ 1 + \operatorname{erf} \left( \frac{\log \alpha - 2.29}{0.89\sqrt{2}} \right) \right]. \quad (17)$$

The choice of mean and standard deviation of the lognormal relationship is governed by experimental results, as shown later.

### Macropore relaxation

Since the relaxation of both micro and macropore is governed by the same Bloch equation (3), we expect the relaxation time of the macropore to also correlate with  $\alpha$ . It is however, found that the macropore relaxation time correlates with the product of  $\alpha$  and square of macroporosity fraction ( $1 - \beta$ ). This is because the product  $(1 - \beta)^2 \alpha$  represents the normalized diffusion time ( $t_d$ ) within the macropore as described below

$$(1 - \beta)^2 \alpha = \frac{((1 - \beta)L_2)^2 / D}{L_1 / \rho\beta} = \frac{t_d}{T_{2,c}} \quad (18)$$

Figure 8 shows the plot of dimensionless relaxation time of the macropore with  $\nu = (1 - \beta)\sqrt{\alpha}$  for different parameter values. Here, the relaxation time is correlated with  $\nu$  instead of its square because  $\nu$  is proportional to the length scale,  $L_2$ , of macropore (equation (18)). We can establish a cubic

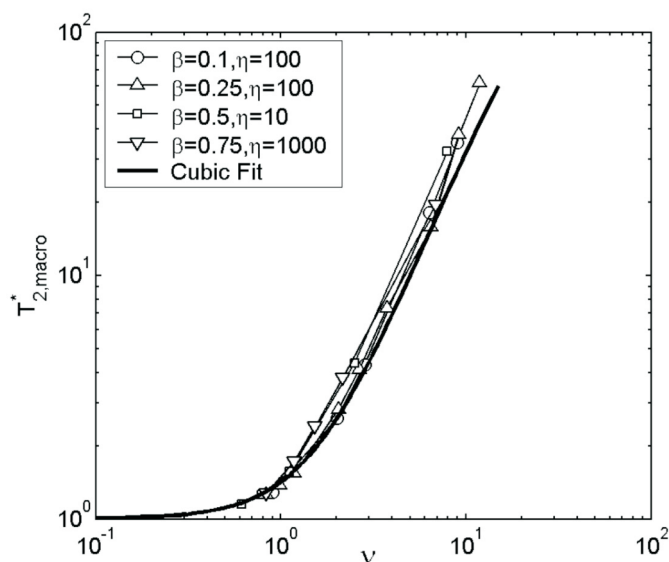


FIG. 8 Dimensionless relaxation time of macropore shows cubic relationship with  $\nu = (1 - \beta)\sqrt{\alpha}$ .

relationship between the dimensionless macropore relaxation time and  $\nu$  as shown in equation (19). The cubic relationship provides a better statistical correlation with the experimental results than a quadratic one. The functional relationship, although fitted to experimental results for sandstones and grainstones as shown later, closely match the simulation results.

$$T_{2,macro}^* = 1 + 0.025\nu + 0.4\nu^2 - 0.009\nu^3 \quad (19)$$

where  $10^{-1} < \nu < 10^1$ .

### SANDSTONES

In this section, we extend the ideas developed in the previous section to describe diffusional coupling in clay-lined pores in sandstones. Straley et al. (1995) modeled the clay flakes as forming micro-channels perpendicular to the pore walls such that each micropore opens to a macropore (Figure 9). The two dimensional structure of the clay-lined pore can be modeled as a periodic array of rectangular flakes arranged along the wall of the macropore (Zhang et al., 2001; Zhang et al., 2003). Since the model is periodic, the relaxation process can be adequately modeled by considering only the symmetry element between two clay flakes. The model is further simplified to the one in Figure 2 by approximating the flakes to be needle shaped with negligible thickness.

#### Pore size distribution

To experimentally validate the theoretical model, the NMR response of North-Burbank (NB) sandstone with pores lined with chlorite flakes is simulated (Trantham and Clampitt, 1977). Analysis of the sandstone cores yielded an average porosity of 0.22 and air/brine permeability of 220 mD. Figure 10 shows the pore throat distribution obtained by mercury porosimetry for one of the cores. The bimodal structure of the pore size distribution arises due to the pres-

ence of pore-lining chlorite flakes. Mercury first invades the macropores giving rise to the peak at larger pore radii. The clay flakes, being closely spaced, are invaded by mercury at high capillary pressures which gives rise to the peak at smaller pore radii.

A lognormal pore throat distribution with mean of  $8 \mu\text{m}$  and standard deviation of  $0.135 \mu\text{m}$  is simulated to approxi-

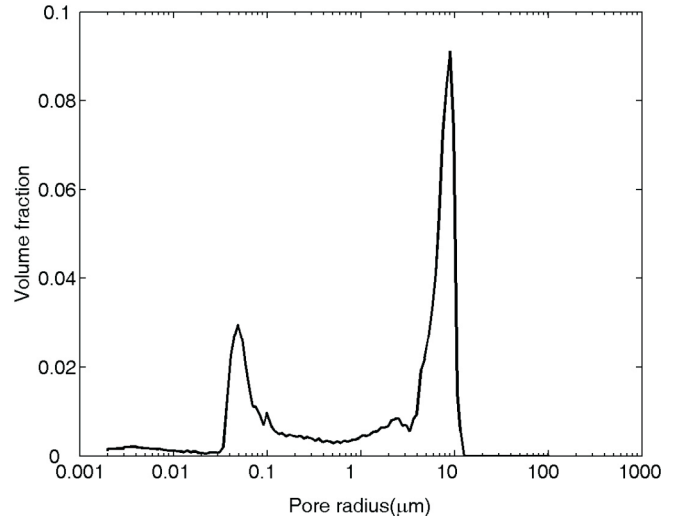


FIG. 10 Pore throat distribution of North-Burbank sandstone obtained using mercury porosimetry. The bimodal structure arises due to pore-lining chlorite clay flakes.

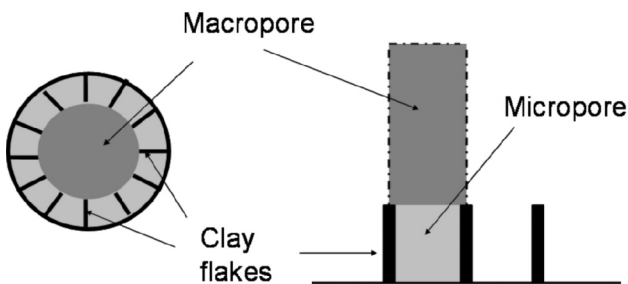


FIG. 9 a) Model of a clay lined pore showing micropores opening to a macropore b) Simplified model with rectangular clays arranged along macropore wall.

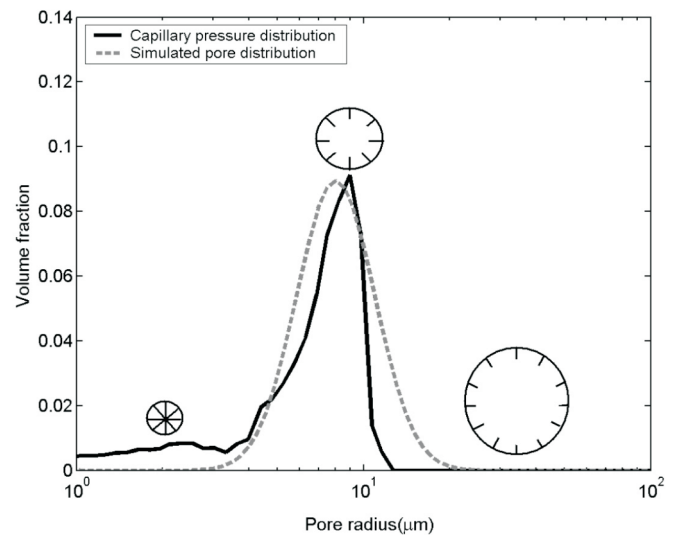


FIG. 11 Simulated lognormal pore size distribution to approximate the distribution of clay-lined macropores. Also shown are the pores with changing proportion of pore volume occupied by the clay flakes.

mate the distribution of macropores (Figure 11). Since mercury porosimetry measures the distribution of pore throats, the distribution of pore bodies is obtained by assuming a fixed pore body to pore throat ratio of 3 (Lindquist et al., 2000). Thus, the most abundant pore has the pore body radius ( $L_2$ ) of  $24 \mu\text{m}$ . Each pore is then modeled to be lined with clay flakes which are assumed to be of constant length and equally spaced in all pores. As a result, the flakes completely occupy the small pores and form a thin rim on the surface of larger pores. The distance between the flakes ( $L_1$ ) is given by the peak at smaller pore radius in the pore size distribution ( $\approx 0.03 \mu\text{m}$ ).

### Numerical solution

In order to solve equation (3) for the decay of magnetization in the  $i^{\text{th}}$  pore, we need three parameters:

1. Microporosity fraction  $\beta_i$
2. Aspect ratio  $\eta_i = L_{2,i}/L_{1,i}$
3. Brownstein number  $\mu_i = \rho L_{2,i}/D$

The parameters in different pores are, however, not totally independent of each other since they are constrained by the assumptions of constant length and equal spacing between clay flakes in all pores. Mathematically, the constraints imply

$$L_{1,i} = L_{1,c} = \text{const.} \quad (20)$$

$$\beta_i L_{2,i} = \beta_c L_{2,c} = \text{const.} \quad (21)$$

where the subscript ‘‘c’’ refers to the characteristic or most abundant pore. If we specify the parameters for the characteristic pore, the parameters for the rest of the pores are calculated by making use of the constraints. Similar to the analysis of a single pore in the previous section, the governing equations (3-5) for each pore are normalized with respect to common characteristic parameters. The spatial variables and time are respectively normalized by the radius and characteristic relaxation time (equation (6)) of the most abun-

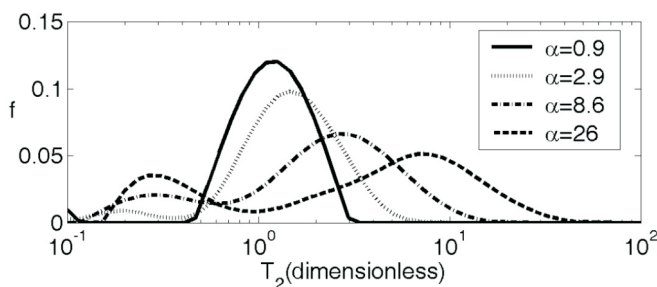


**FIG. 12** Simulated  $T_2$  distributions for a pore size distribution with  $\beta_c = 0.3$  and  $\eta_c = 100$  showing transition from unimodal to bimodal distribution with increase in  $\bar{\alpha}$ .

dant pore. The normalized equations are then solved for the decay of magnetization in each pore individually. The magnetization in the entire pore structure is computed by interpolating the individual magnetization values at some common values of time and then summing them over the entire volume. The total magnetization ( $M_{tot}$ ) in the pore structure is given as

$$M_{tot}(t) = \sum_i^{N_p} V_{p,i} M_i(t) \quad (22)$$

where  $N_p$  is the number of pores,  $V_{p,i}$  is the volume fraction of the  $i^{\text{th}}$  pore and  $M_i$  is the magnetization in the  $i^{\text{th}}$  pore at dimensionless time  $t$ . The  $T_2$  distribution for the pore structure is obtained by fitting a multi-exponential distribution to the total magnetization.

### Results

Since each pore in the pore size distribution has a different value of  $\alpha$ , a volume averaged  $\bar{\alpha}$  for the distribution is defined as

$$\bar{\alpha} = \sum_i \alpha_i V_{p,i} = \sum_i \beta_i \eta_i \mu_i V_{p,i} \quad (23)$$

The simulated  $T_2$  distributions for the pore size distribution with typical values of  $\beta_c$  and  $\eta_c$  ( $\beta_c = 0.3$  and  $\eta_c = 100$ ) are shown in Figure 12 as a function of  $\bar{\alpha}$ . The  $T_2$  distribution changes from unimodal to bimodal with the increase in the values of  $\bar{\alpha}$ . This is because when  $\bar{\alpha} < 1$ , the pores are in total coupling regime and each pore relaxes single exponentially with the dimensionless relaxation time,  $T_{2,i}$ , given as

$$T_{2,i} = \frac{(V/\rho S)_i}{T_{2,c}} = \frac{\beta_c}{\beta_i} = \frac{L_{2,i}}{L_{2,c}} \quad (24)$$

Thus, for  $\bar{\alpha} < 1$ , the  $T_2$  distribution exactly replicates the unimodal lognormal distribution of the pore radii. As the pores enter the intermediate coupling regime ( $\bar{\alpha} > 1$ ), a fraction of microporosity starts relaxing independently of the macroporosity, thereby giving the  $T_2$  distributions a bimodal shape.

### Experimental verification

The simulations with characteristic parameters representative of the core properties are compared with the experimental results for North Burbank. The value of  $\beta_c$  is calculated such that the microporosity fraction of the simulated pore size distribution corresponds to the irreducible water saturation, i.e

**TABLE 1** Characteristic parameters for the simulations for three NB cores.

Core	$\beta_c$	$\eta_c$	$\mu_c$	$\bar{\alpha}$
NB1	0.3	800	0.048	12.2
NB2	0.28	800	0.065	15
NB3	0.21	800	0.094	16.6

$$\sum_i^{N_p} \beta_i V_{p,i} = S_{w,irr} \quad (25)$$

$$\Rightarrow \beta_c = \frac{S_{w,irr}}{L_{2,c} \sum_i^{N_p} \frac{V_{p,i}}{L_{2,i}}} \quad (26)$$

The aspect ratio  $\eta_c$  is calculated from the ratio of macropore and micropore radii obtained from mercury porosimetry. The third parameter  $\mu_c$  is specified such that the simulations best match with the experimental results.

Figure 13(a) shows the comparison of the  $T_1$  distribution of a water-saturated NB core with the corresponding simu-

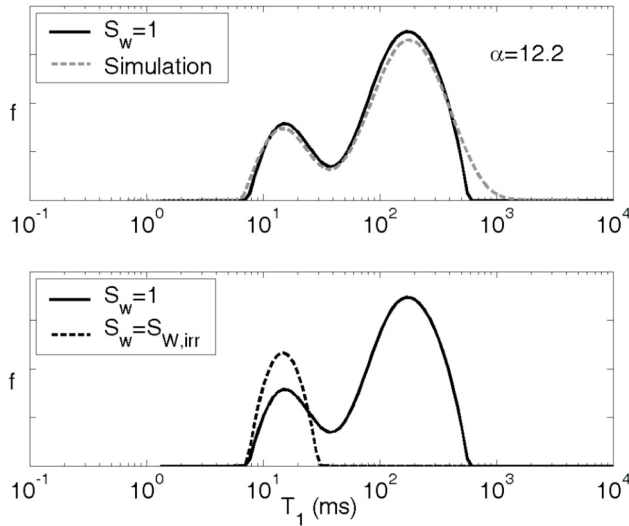


**FIG. 13** a) Comparison of simulated and experimental  $T_1$  distributions for 100% water saturated NB core. The value of  $\bar{\alpha}$  indicate intermediate coupling regime for water saturated core. b) Comparison of  $T_1$  distributions of the core at 100% water saturation and at irreducible saturation. Increase in the amplitude of the micropore peak at irreducible saturation also illustrates intermediate coupling regime.

lated distribution. The comparison is made with the  $T_1$  (instead of the  $T_2$ ) distributions since the  $T_2$  relaxation is additionally influenced by diffusion in internal gradients induced by chlorite flakes (Zhang et al., 2001; Zhang et al., 2003). Diffusional coupling, however, affects both  $T_1$  and  $T_2$  relaxation since it arises due to diffusion between pores of different surface-to-volume ratios. The characteristic parameters for the simulations are shown in Table 1. The dimensionless simulated distributions are dimensionalized by choosing  $T_{2,c} = 50$  ms, which gives the best overlay of the simulated and experimental distributions. The value of  $\bar{\alpha}$  ( $= 12.2$ ) indicates that the micro and macropores are in intermediate coupling regime. The intermediate coupling regime is also demonstrated in Figure 13(b), which shows the comparison of  $T_1$  distributions of the core at 100% water saturation and at irreducible saturation. An increase in the amplitude of the micropore peak is observed at irreducible saturation. This increase in the amplitude is observed because at irreducible saturation, there is no diffusional exchange of the fluid in micro and macropores and the fluid relaxes with a rate proportional to the surface-to-volume ratio of the micropores. However, at 100% water saturation, a fraction of the fluid in micropores is exchanging with the macropores. The apparent volume of the fluid in micropores is larger thereby resulting in a smaller surface to volume ratio, which increases its relaxation time.

Figure 14(a) shows the plot of the amplitude of the micropore peak at 100% water saturation normalized with

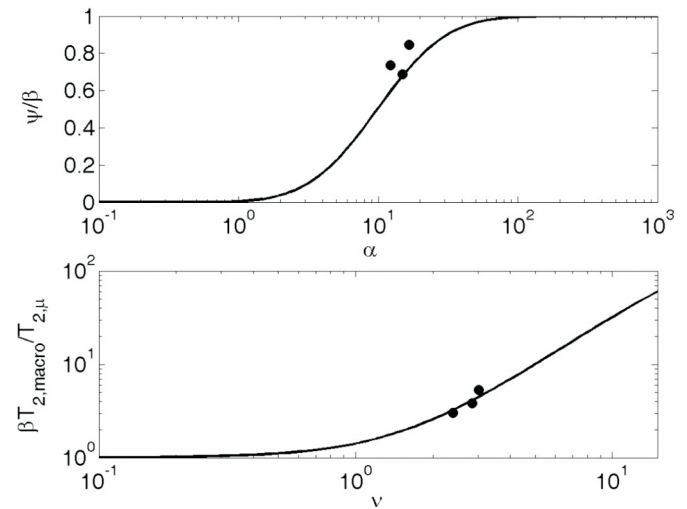


**FIG. 14** a) Plot of independent microporosity fraction with  $\alpha$  for three water saturated NB cores. The measurements fall in intermediate coupling regime of the lognormal relationship of equation (17). b) Plot of normalized relaxation time with  $v = (1 - \beta)\sqrt{\bar{\alpha}}$  for the three cores.

the total microporosity fraction with  $\bar{\alpha}$  for three NB cores considered in this study. The simulation parameters required for the calculation of  $\bar{\alpha}$  for the cores are also mentioned in Table 1. The measurements fall on the intermediate coupling regime of the lognormal relationship (equation (17)) for all cores. Figure 14 (b) shows that the cubic relationship (equation (19)) for the normalized macropore relaxation time also holds for the cores. In the figure, the relaxation time of the macropore is normalized by a characteristic relaxation time defined by equation (8).

To explore another coupling regime, measurements were made with dry cores saturated with hexane. Higher extent of coupling is expected with hexane than with water due to higher diffusivity and lower surface relaxivity for hexane. The lower surface relaxivity for hexane is due to intrinsic smaller hydrocarbon relaxivity of the sandstone surfaces (Chen et al., 2005). Figure 15 shows the  $T_1$  distribution of the hexane saturated core and the corresponding simulated distribution. The dimensionless simulated distribution is dimensionalized by choosing  $T_{2,c} = 450$  ms. In this case, the  $T_1$  distribution is unimodal implying the merger of the micro and macropore peak. The smaller value of  $\bar{\alpha}$  suggest stronger coupling for hexane than for water as can be seen by comparing the values in Figures 13 and 15 respectively.

#### Estimation of surface relaxivity

The values of the surface relaxivity for the cores can be calculated from the corresponding values of  $\bar{\alpha}$ . For the values of parameters  $L_{2,c} = 24 \mu\text{m}$ ,  $L_1 = 0.03 \mu\text{m}$ , diffusivity for water and hexane  $D_w = 2.5 \times 10^{-5} \text{ cm}^2/\text{s}$  and  $D_H = 4.2 \times 10^{-5} \text{ cm}^2/\text{s}$  (Reid et al., 1987), the average value of relaxivity is found to be  $7.1 \mu\text{m}/\text{sec}$  for water and  $1.6 \mu\text{m}/\text{sec}$  for hexane. The lower surface relaxivity of hexane is not due to water-wetness of the sandstone since hexane was in direct contact with the mineral surfaces and no water was present. Another estimate of relaxivity is obtained by comparing the cumulative pore size distributions obtained

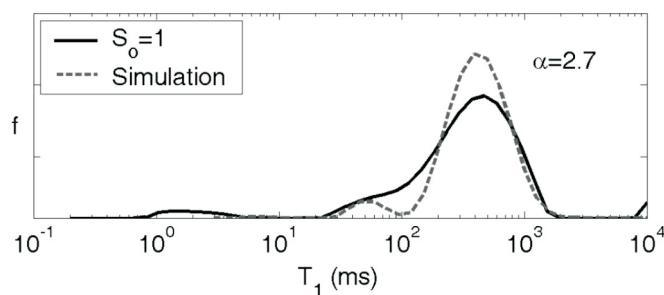


**FIG. 15** Comparison of simulated and experimental  $T_1$  distributions for hexane saturated NB core. The value of  $\bar{\alpha}$  indicates strong coupling for hexane saturated core.

by  $T_1$  relaxation and mercury porosimetry. However, the estimates from the latter method are about three times ( $20 \mu\text{m}/\text{sec}$  for water) as high as those calculated from simulations. This is because mercury porosimetry does not take into account the large surface area provided by the clay flakes in the estimation of relaxivity.

### GRAINSTONES

The analysis of the first section on diffusional coupling is also applied to describe pore coupling in grainstone carbonates. Ramakrishnan et al. (1999) modeled the grainstones as microporous spherical grains surrounded by intergranular pores. This three dimensional model can be mapped into a two-dimensional model of a periodic array of slab-like grains separated by intergranular macropores as shown in Figure 16. We transform this model to the one in Figure 2 by neglecting the thickness of grain between the micropores and assuming the pores to be linear in shape. Note that in this model relaxation at the outer surface of the grains is neglected. We are justified in making these assumptions if the surface-to-volume ratio of the micropore is much larger compared to the external surface-to-volume ratio of the spherical grains.

#### Coupling parameter for grainstones

The transformation of the spherical grain model to the 2-D model in Figure 2 enables us to define a coupling parameter for grainstones through a mapping of characteristic parameters. In Figure 2,  $L_1$  was defined to be the half-width of the micropore. Hence for microporous grains,  $L_1$  corresponds to the radius of the micropore ( $R_\mu$ ) i.e.

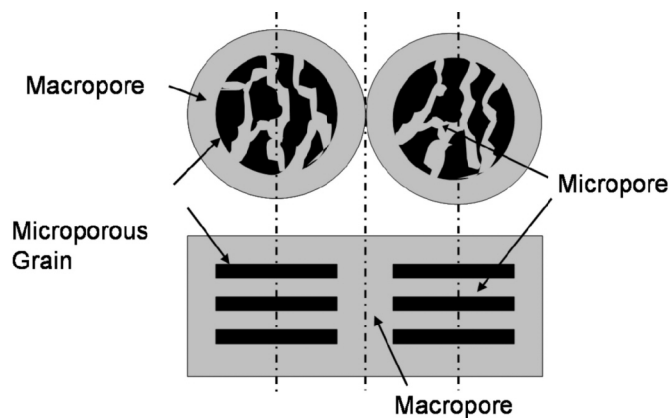


**FIG. 16** Pore coupling model in grainstone systems. The three-dimensional model can be mapped to a two-dimensional model of periodic array of microporous grains separated by macropores.

$$L_1 = R_\mu . \quad (27)$$

Also, as a first approximation,  $L_2$  can be taken to be equal to the grain radius ( $R_g$ )

$$L_2 = R_g . \quad (28)$$

Substituting equations (27) and (28) in equation (11), we get the definition of  $\alpha$  for grainstones as

$$\alpha_{grain} = \frac{\rho\beta R_g^2}{DR_\mu} \quad (29)$$

$\alpha_{grain}$ , thus, shows a quadratic dependence on the grain radius and inverse dependence on the micropore radius. This definition suggests that grainstones with large grain radius and/or small micropore radius are expected to show less effect of diffusional coupling.

The above definition of coupling parameter also helps us to understand the analysis of grainstone model developed by Ramakrishnan et al. (1999). They suggested that in the case when the decay of magnetization in macropore occurs on a time scale much larger than that for the decay of magnetization in micropore, relaxation in the coupled geometry can be expressed as a bi-exponential decay with amplitudes representative of the micro and macroporosity fractions as shown

$$M(t) = \phi_m \exp\left(-\frac{\rho_a t}{V_{sm}}\right) + (\phi - \phi_m) \exp\left(-\frac{t}{T_{2,\mu}}\right). \quad (30)$$

In the above equation,  $V_{sm}$  is the macropore volume-to-surface ratio,  $\phi$  and  $\phi_m$  are the total porosity and macroporosity respectively and  $\rho_a$  is the apparent relaxivity for the macropore. This bi-exponential model is valid when the diffusion length of magnetization within the microporous grain is much smaller than the grain radius, i.e.

$$\sqrt{\frac{DT_{2,\mu}}{\phi_\mu F_\mu}} \ll R_g \quad (31)$$

where  $F_\mu$  is the formation factor. We can understand the above condition by substituting the expressions for the parameters from the two dimensional model of Figure 16. The relaxation rate of the micropore is related to the micropore radius, assuming cylindrical pores, as

$$\frac{1}{T_{2,\mu}} = \rho \left(\frac{S}{V}\right)_\mu = \frac{2\rho}{R_\mu}. \quad (32)$$

The microporosity fraction  $\beta$  is equal to the product of grain

fraction  $(1 - \phi_m)$  and porosity of grains  $\phi_m$  normalized by total porosity  $\phi$ ,

$$\beta = \frac{\phi_\mu(1 - \phi_m)}{\phi}. \quad (33)$$

Substituting the expressions for  $1/T_{2,\mu}$  and  $\phi_\mu$  from equations (32) and (33) in (31), we get

$$\sqrt{\frac{DR_\mu(1 - \phi_m)}{2\rho\beta\phi F_\mu}} \ll R_g \quad (34)$$

$$\Rightarrow \alpha_{grain} \equiv \frac{\rho\beta R_g^2}{DR_\mu} \gg \frac{(1 - \phi_m)}{2\phi F_\mu}. \quad (35)$$

The above condition implies that the micropore relaxes independently of the macropore for large values of  $\alpha$ , which is the same condition for the decoupled regime obtained for our model. However, for typical values of grainstone parameters, the value of apparent relaxivity is much larger than the micropore relaxivity (Ramakrishnan et al., 1999). Thus, even though the surface-to-volume ratio of macropore is significantly smaller than that of the micropore, diffusional coupling can result in the decay of macro and micropore at comparable time scales. For such cases, the pores are in intermediate coupling regime and the amplitudes of the bi-exponential fit are not representative of the actual micro and macroporosity fractions as was observed in the numerical simulations of Ramakrishnan et al. (1999).

### Experimental validation

In order to experimentally validate the grainstone model, NMR response of three systems — microporous chalk, silica gels and alumino-silicate molecular sieves — was studied as a function of grain radius. These systems with varying physical properties help us to systematically analyze the effect of different governing parameters on pore coupling. The physical properties of the systems are listed in Table 2.

#### Chalk

Crushed microporous chalk (Crayola) was sieved into five fractions with average grain radii of 335  $\mu\text{m}$ , 200  $\mu\text{m}$ , 112  $\mu\text{m}$ , 56  $\mu\text{m}$  and 11  $\mu\text{m}$ . Known quantities of sorted fractions were water saturated in 1" by 1" Teflon sleeves whose bases were sealed with a covering of Teflon tape. After measuring the NMR response at 100% water saturation, the systems were centrifuged in a Beckman rock core centrifuge at an air/water capillary pressure of 100psi for 3 hours to drain the macropores. The Teflon base is permeable to water but prevents any grain loss during centrifugation.

Note that even though the sieve fractions are unconsolidated, they have irreducible intragranular microporosity which is not displaced on capillary drainage.

The  $T_2$  distributions of the five fractions at 100% water saturation and the corresponding distributions at irreducible saturation are shown in Figure 17. The values of  $\alpha_{grain}$  calculated using equation (29) and  $\mu_{grain}(=\rho R_g/D)$  are also mentioned for each sieve fraction. We can see that for the

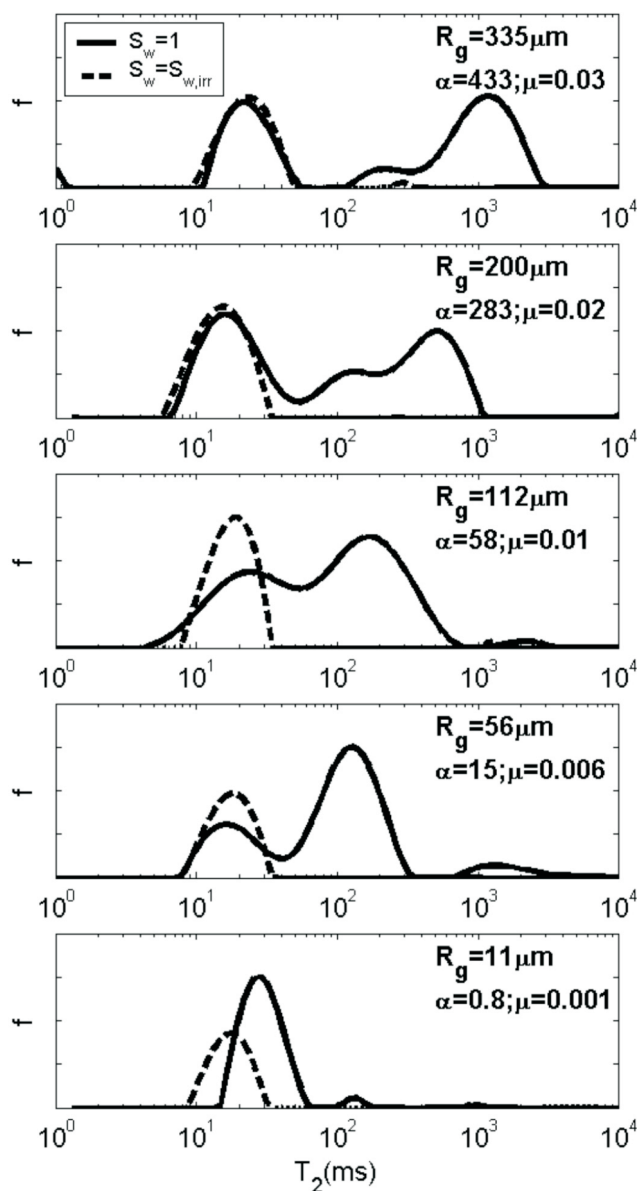


FIG. 17  $T_2$  distributions of microporous chalk as a function of grain radius. The transition from decoupled ( $R_g = 335 \mu\text{m}$ ) to total coupling regime ( $R_g = 11 \mu\text{m}$ ) is predicted by the values of  $\alpha$ .

TABLE 2 Physical properties of the grainstone systems.

	Chalk	Silica Gels	Molecular Sieves
BET Surface Area ( $\text{m}^2/\text{g}$ )	4.1	300	20
Micropore Diameter ( $\text{\AA}$ )	185	150	4
Surface Relaxivity ( $\mu\text{m}/\text{sec}$ )	0.27	0.06	0.04

two coarsest fractions ( $R_g = 335 \mu\text{m}$  and  $200 \mu\text{m}$ ), the  $T_2$  distributions show distinct peaks for micro and macropores and the area under the micropore peak is the same as that at irreducible conditions. This implies that the systems are in the decoupled regime, which is verified by large values of  $\alpha_{grain}$ . The effect of coupling becomes more pronounced for systems with  $R_g = 112 \mu\text{m}$  and  $56 \mu\text{m}$ , which show a build up of micropore peak amplitude at irreducible saturation. The amplitude of the micropore peak increases because at irreducible condition, there is no diffusional exchange of the fluid in micro and macropores. Thus, the relaxation rate of the fluid is proportional to the surface-to-volume ratio of the micropores. However, at 100% saturation, part of the fluid in micropores is in diffusional exchange with the macropores. Thus, the apparent volume of the fluid in micropores is larger which decreases its relaxation time. This is the same explanation given by Coates et al. (1998) for the observed increase in amplitude of short  $T_2$  components at irreducible saturation in sandstone cores. The values of  $\alpha_{grain}$  for  $R_g = 112 \mu\text{m}$  and  $56 \mu\text{m}$  correspond to the intermediate coupling regime and thus, quantitatively supports the explanation. The unimodal  $T_2$  distribution of the finest fraction ( $R_g = 11 \mu\text{m}$ ) at 100% water saturation shows that the system is in total coupling regime ( $\alpha_{grain} = 0.8 < 1$ ).

#### Silica gels

A homologous series of silica gels (provided by Sigma-Aldrich) with grain radii of  $168 \mu\text{m}$ ,  $55 \mu\text{m}$  and  $28 \mu\text{m}$  constituted the second system. Figure 18 shows the  $T_2$  distributions at 100% water saturation and at irreducible saturation for the three fractions. Similar to the response of chalk, the distributions change from being bimodal to unimodal with the decrease in particle diameter indicating increased coupling. The values of  $\alpha_{grain}$  suggest intermediate coupling regime for the two coarsest fractions ( $R_g = 168 \mu\text{m}$  and  $55 \mu\text{m}$ ) and total coupling regime for the finest fraction ( $R_g = 28 \mu\text{m}$ ).

Molecular sieves

Alumino-Silicate molecular sieves with nominal pore diameter of  $4\text{\AA}$ , supplied by Fisher Chemicals, was crushed and sieved into four fractions with average grain radii of  $200\ \mu\text{m}$ ,  $112\ \mu\text{m}$ ,  $56\ \mu\text{m}$  and  $16\ \mu\text{m}$ . The  $T_2$  distributions of the four fractions are shown in Figure 19 at 100% water saturation and at irreducible saturation. The response shows similar trend of narrowing  $T_2$  distributions with decrease in the grain diameter. An increase in amplitude of the micropore peak at irreducible conditions is observed for fractions with  $R_g = 56\ \mu\text{m}$  and  $16\ \mu\text{m}$ , which shows that these fractions are in intermediate coupling regime. The values of  $\alpha_{grain}$  for the respective fractions predict the transition of the coupling regimes.

Figure 20 shows that the lognormal and cubic relationships of equations (17) and (19) also hold for the three systems, thereby establishing the validity of the grainstone model.

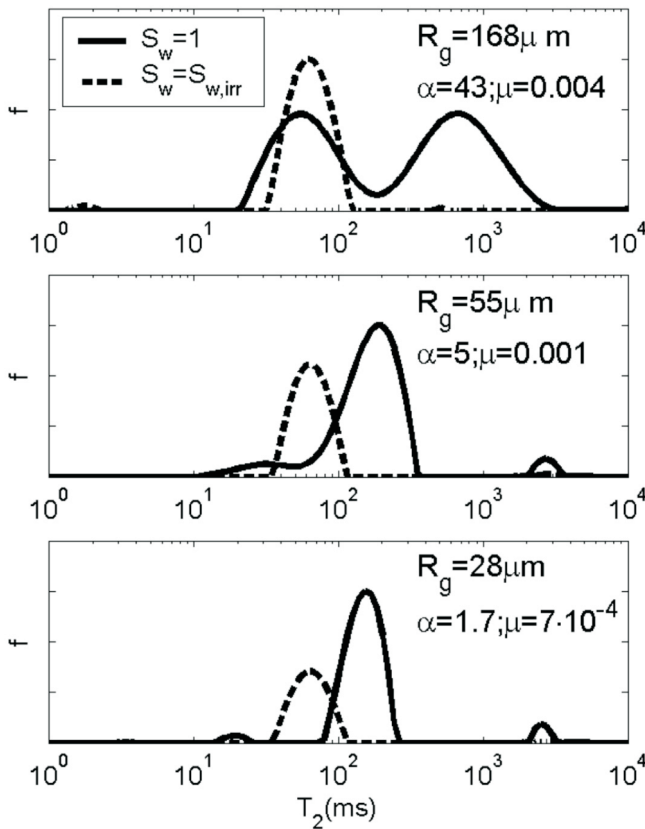


FIG. 18  $T_2$  distributions of silica gels as a function of grain radius. The transition from almost decoupled ( $R_g = 168\ \mu\text{m}$ ) to total coupling regime ( $R_g = 55\ \mu\text{m}$ ) is predicted by the values of  $\alpha$ .

ESTIMATION OF IRREDUCIBLE WATER SATURATION

The sharp cutoff method of estimating  $S_{w,irr}$  employs a lithology-specific sharp  $T_{2,cutoff}$  to partition the  $T_2$  spectrum into free fluid and bound fluid saturations. For formations with diffusively coupled micro and macropores, the use of a sharp cutoff may give incorrect estimates since in such cases the direct relationship between pore size and  $T_2$  distribution no longer holds.

In the case of pore coupling, the estimation of  $S_{w,irr}$  amounts to the calculation of microporosity fraction  $\beta$  for a given  $T_1$  or  $T_2$  distribution at 100% water saturation. The solution of this inverse problem is obtainable by making use of the correlations for independent microporosity fraction and normalized macropore relaxation time (equations (17) and (19)). Three parameters are required for the solu-

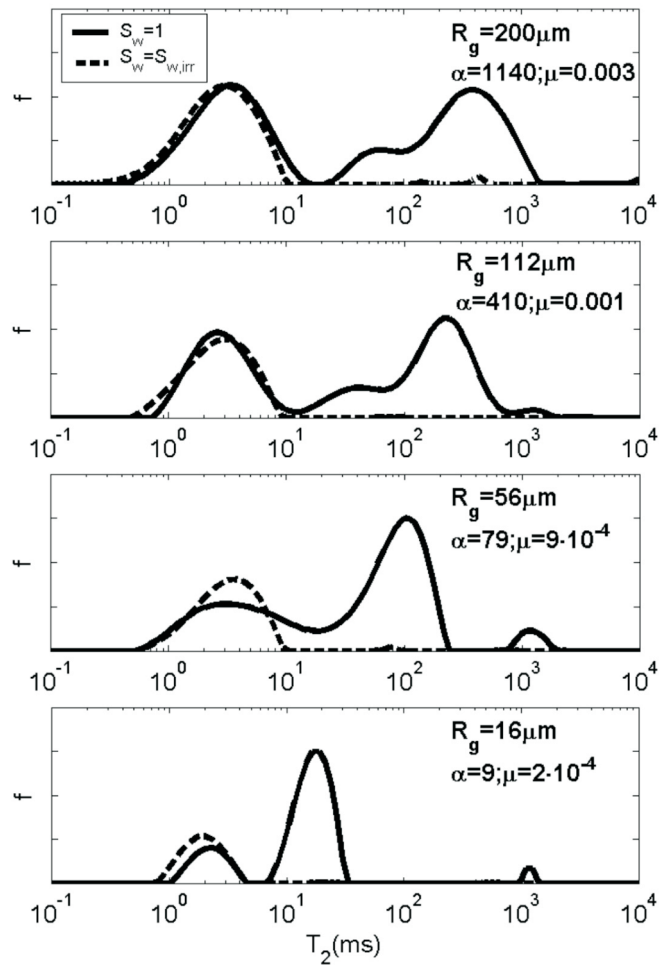


FIG. 19  $T_2$  distributions of alumino-silicate molecular sieves as a function of grain radius. The values of  $\alpha_{grain}$  for the sieve fractions predict the transition of the coupling regimes.

tion: micropore peak amplitude ( $\psi$ ), relaxation time of the micropore ( $T_{2,\mu}$ ) and relaxation time of the macropore ( $T_{2,macro}$ ). It is assumed that  $T_{2,\mu}$  is known from laboratory core analysis and is same for the formation. This assumption is justified if the formation has similar relaxivity and micropore structure as the cores. From the  $T_2$  spectrum at 100% water saturation, the values of  $\psi$  and  $T_{2,macro}$  can be calculated as the area under the micropore peak and the relaxation time of the mode of the macropore peak, respectively. Hence, for the estimated parameter values, the correlations can be simultaneously solved for the values of  $\alpha$  and  $\beta$ . Graphically, the solution involves determining the intersection point of contours of  $\psi$  and  $T_{2,macro}/T_{2,\mu}$  on the  $\alpha$  and  $\beta$  parameter space as shown in Figure 21. The values of con-

tour lines for  $T_{2,macro}/T_{2,\mu}$  differ by a factor of 2 and those for  $\psi$  differ by 0.1. The coordinates of the intersection point of the contours for experimentally determined values of  $\psi$  and  $T_{2,macro}/T_{2,\mu}$  estimates the value of  $\alpha$  and  $\beta$  for the formation. For a unimodal distribution with a zero value of  $\psi$  (total coupling regime), the microporosity fraction can be calculated from the ratio of the relaxation times of micro and macropore, i.e.

$$\beta = \left( \frac{T_{2,\mu}}{T_{2,macro}} \right), \psi = 0. \quad (36)$$

In this case, the value of  $\alpha$  is indeterminate and can be anything less than 1. This is because as  $\psi$  approaches 0, the contours for  $T_{2,macro}/T_{2,\mu}$  asymptote to the reciprocal  $\beta$  value independent of  $\alpha$ . (Note  $\psi = 0$  implies totally coupled micro and macropore and not necessarily the absence of microporosity).

Figure 22 shows the comparison of the calculated values of  $\beta$  and  $\alpha$  with the values determined experimentally for the grainstone and sandstone systems. An average value of  $T_{2,\mu}$  obtained from the individual values for different sieve fractions or cores is used for calculations. The estimates lie within an average absolute deviation of 4% and 11% for  $\beta$  and  $\alpha$ , respectively. This indicates that the technique is applicable to all the systems studied irrespective of the properties and coupling regimes.

### Unification of spectral and sharp cutoff theory

The estimation of  $S_{w,irr}$  using spectral or tapered  $T_{2,cutoff}$  is

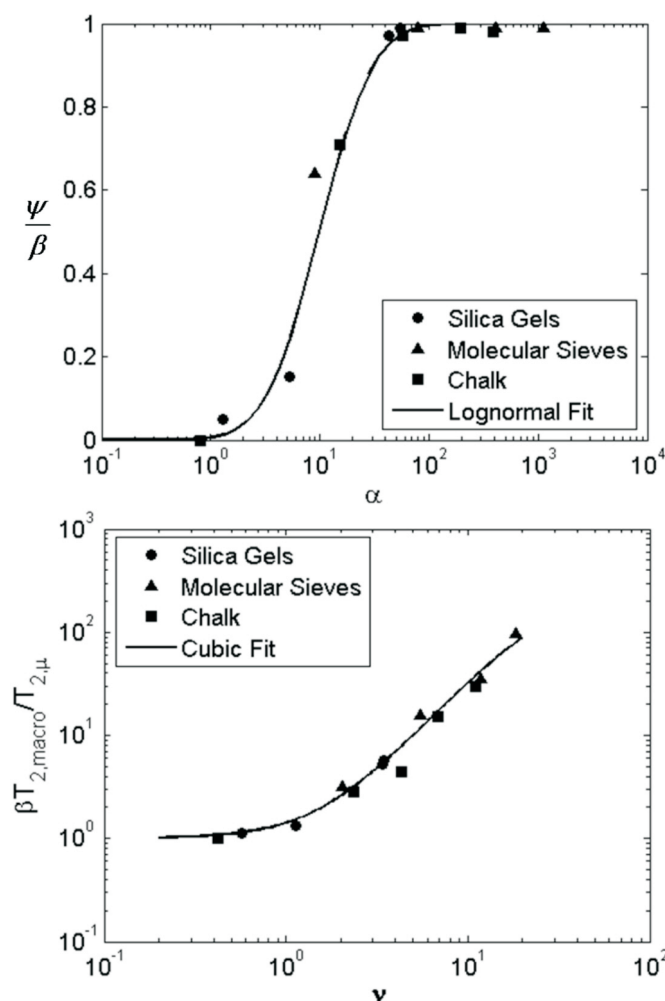


FIG. 20 Plot of independent microporosity fraction with  $\alpha$  for model grainstone systems (Upper panel). Plot of normalized macropore relaxation time with  $v = (1 - \beta)\sqrt{\alpha}$  for the systems (Lower Panel). The experimental points follow the lognormal and cubic relationships of equations (17) and (19).

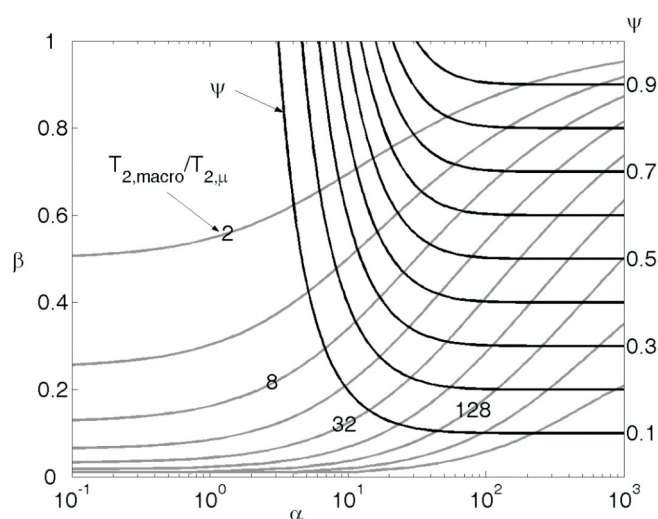


FIG. 21 Contour plots of correlations for  $\psi$  and  $T_{2,macro}/T_{2,\mu}$  in  $\alpha$  and  $\beta$  parameter space. Intersection point of contours estimates the value of  $\alpha$  and microporosity fraction for the formation.

based on the premise that each pore size has its own inherent irreducible water saturation. The fraction of bound water associated with each pore size is defined by a weighting function  $W(T_{2,i})$  where  $0 \leq W(T_{2,i}) \leq 1$ . The  $S_{w,irr}$  is then given as

$$S_{w,irr} = \sum_j^n W_j f_j \quad (37)$$

where  $n$  is the number of bins and  $f_j$  is the amplitude of each bin. The weighting factors are determined using empirical permeability models or cylindrical pore models (Coates et al., 1998; Kleinberg and Boyd, 1997).

An implicit assumption of the above-mentioned technique is that the producible and irreducible fractions of each pore have same relaxation time at 100% water saturation. However, the analysis of a single pore (see section on diffusional coupling) shows that micro and macropore can communicate through decoupled and intermediate coupling regimes as well. Thus, in a general coupling scenario, the response of the pore shows distinct peaks for micro and macropore with amplitudes  $\psi$  and  $(1 - \psi)$  respectively. The amplitude  $\psi$  can vary from 0 to  $\beta$  depending on the coupling regime. Therefore, the portion of the microporosity coupled with the macropore divided by the macropore amplitude is given as

$$\Phi\left(\frac{T_{2,macro}}{T_{2,\mu}}, \alpha\right) = \frac{\beta - \psi}{1 - \psi} \quad (38)$$

$\Phi$  is a function of the ratio of macro to micropore relaxation times ( $T_{2,macro}/T_{2,\mu}$ ) and  $\alpha$  which determines the microporosity portion coupled with the macropore response. As  $\alpha$  increases, the extent of pore coupling decreases and thus, the microporosity fraction coupled with the macropore response also decreases. Figure 23 show the plot of  $\Phi$  with ( $T_{2,macro}/T_{2,\mu}$ ) for different values of  $\alpha$ . The procedure for estimating  $\Phi$  as a function of ( $T_{2,macro}/T_{2,\mu}$ ) is as follows. For a known value of  $\alpha$ ,  $\Phi$  is calculated from equation (38) for several values of  $\beta$  using equation (17). Similarly,  $T_{2,macro}/T_{2,\mu}$  is calculated for the known  $\alpha$  and same values of  $\beta$  by substituting the expression of  $T_{2,c}$  from equation (8) in equation (19)

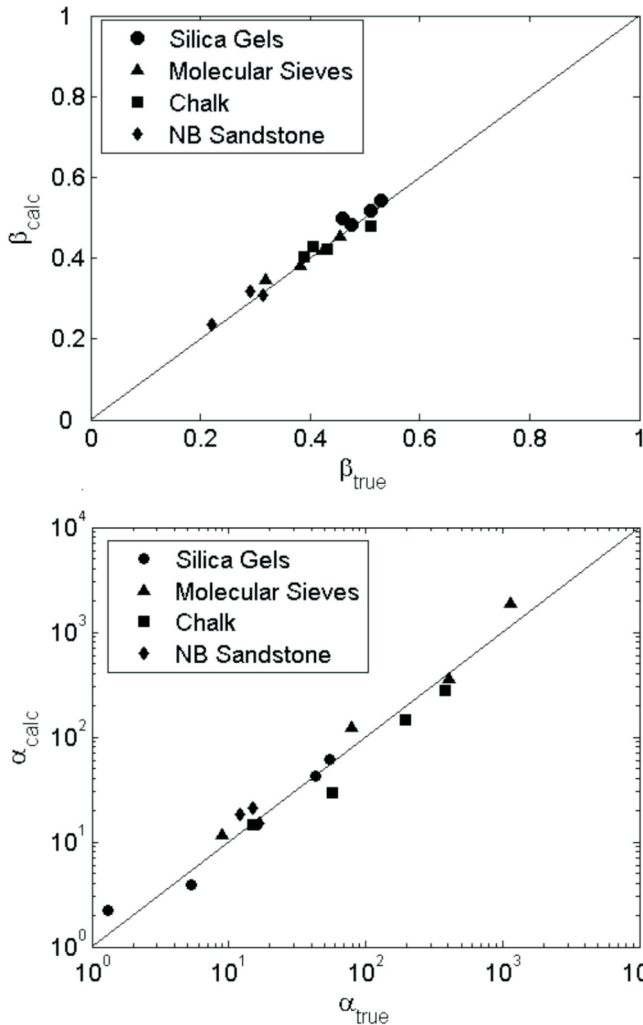


FIG. 22 Comparison of calculated and experimentally measured values of  $\alpha$  and  $\beta$  for the grainstone and sandstone systems. The values are estimated within 11% and 4% error respectively.

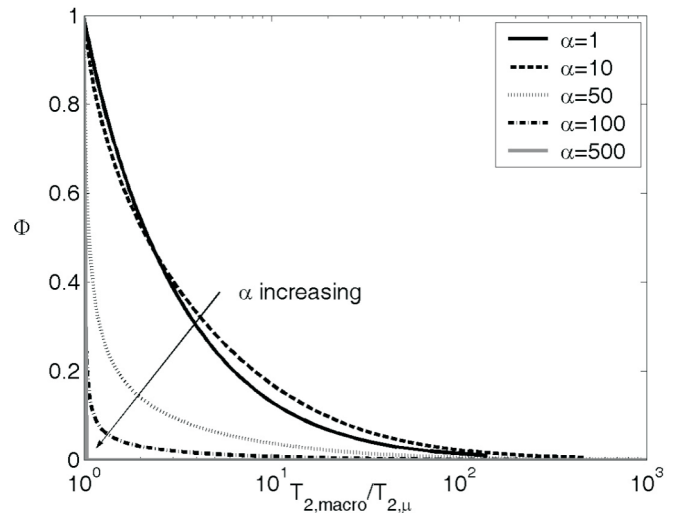


FIG. 23 Plot of  $\Phi$  versus  $T_{2,macro}/T_{2,\mu}$  for different  $\alpha$ . A spectral or tapered cutoff is required for the estimation of irreducible saturation in intermediate coupling regime. A sharp cutoff is applicable for decoupled regime.

$$\frac{T_{2,macro}}{T_{2,\mu}} = \frac{1 + 0.025\nu + 0.4\nu^2 - 0.009\nu^3}{\beta}. \quad (39)$$

Thus, the values of  $\Phi$  and  $(T_{2,macro}/T_{2,\mu})$  for the same  $\alpha$  and  $\beta$  can be cross-plotted as shown in Figure 23. The curves show that a spectral or tapered cutoff is required for the estimation of irreducible saturation in total or intermediate coupling regime. As  $\alpha$  increases,  $\Phi$  decreases for same  $T_{2,macro}/T_{2,\mu}$  indicating lesser correction for diffusional coupling is required for larger  $\alpha$ . Once the pores are decoupled, a sharp cutoff is suitable for estimating irreducible fraction as illustrated by sharp fall of  $\Phi$  curve to zero for all  $\alpha > 200$ . This could also probably explain the suitability of a single lithology-specific  $T_{2,cutoff}$  for estimating irreducible saturations when the formation is in decoupled regime irrespective of the properties. More experiments are, however, needed to prove this postulate.

### CONCLUSIONS

The direct correspondence between pore size and  $T_2$  distribution fails if pores of different sizes are coupled by diffusion. A theoretical model is developed that provides a quantitative understanding of the effect of physical and geometrical parameters on diffusional coupling. It is shown that the Brownstein number fails to characterize relaxation regimes in coupled pores due to its dependence on macropore length scale only. Instead, a coupling parameter ( $\alpha$ ) is introduced that is defined as the ratio of the characteristic relaxation rate of the coupled pore to the rate of diffusional mixing of magnetization between micro and macropore.  $\alpha$  includes the contribution of both micro and macropore to the total surface-to-volume ratio and provides a better measure to quantify diffusional coupling. Depending on the value of  $\alpha$ , micro- and macropores can communicate through total coupling, intermediate coupling or decoupled regimes.

An inversion technique for the estimation of microporosity fraction and  $\alpha$  for formations with unknown geometrical parameters is also introduced. The required parameters for the estimation are easily obtainable from laboratory core analysis and the  $T_2$  (or  $T_1$ ) spectrum at 100% water and irreducible saturation. It is assumed that the relaxation time of micropore is the same in the cores and in the field.  $\alpha$  also provides a quantitative basis for the application of spectral or sharp cutoffs. A sharp  $T_{2,cutoff}$  is applicable for the estimation of irreducible microporosity fraction in the decoupled regime. However, a spectral or tapered cutoff is required in total coupling or intermediate coupling regimes. This is because in these regimes and at 100% water saturation, the amplitudes of micro and macropore peaks of the  $T_2$  distribution are not representative of true

porosity fractions. Experiments with sandstones and microporous grainstones show that the application of inversion technique provides accurate estimate of microporosity fraction in all coupling regimes.

### NOMENCLATURE

$D$	Self diffusion coefficient
$f$	Amplitude of the $T_2$ bins
$L_1, L_2$	Length scales of micro and macropore, respectively
$M$	Magnetization
$R_g$	Grain radius
$R_\mu$	Micropore radius
$S_{w,irr}$	Irreducible water saturation
$S/V$	Surface to Volume ratio of pore
$t$	Time
$T_2$	Transverse relaxation time
$T_{2,\mu}, T_{2,macro}$	Transverse relaxation time of micro and macropore, respectively
$T_{2B}$	Bulk transverse relaxation time
$V_p, N_p$	Volume fraction and number of pores
$W$	Weight fraction of each $T_2$ bin in the SBVI model
$\rho, \rho_a$	True and Apparent surface relaxivity
$x, y$	Spatial variables
$\alpha$	Coupling parameter
$\beta$	Microporosity fraction
$\eta$	Aspect ratio of the pore
$\mu$	Brownstein number
$\lambda$	Regularization parameter
$\psi$	Micropore peak amplitude
$\phi, \phi_m, \phi_\mu$	Total, macro and microporosity, respectively

### ACKNOWLEDGMENTS

The authors would like to acknowledge the Consortium on Processes in Porous Media and US DOE DE-PS26-04NT15515 for financial support. We thank James Howard from ConocoPhillips for providing North Burbank samples and Chuck Devier from PTS for making mercury porosimetry and permeability measurements.

### REFERENCES

- Brownstein, K. R. and Tarr, C. E., 1979, Importance of classical diffusion in NMR studies of water in biological cells: *Physical Review A*, vol. 19, no. 6, p. 2446–2453.
- Coates, G. R., Marschall, D., Mardon, D., and Galford, J., 1998, A new characterization of bulk-volume irreducible using magnetic resonance: *The Log Analyst*, vol. 39, no. 1, p. 51–63.
- Chen, J., Hirasaki, G. J., and Flaum, M., 2006, NMR wettability indices: Effect of OBM on wettability and NMR responses:

*Journal of Petroleum Science and Engineering*, vol. 52, no. 1, p 161–171.

Dunn, K. J., LaTorraca, G. A., Warner, J. L., and Bergman, D. J., 1994, On the calculation and interpretation of NMR relaxation time distributions, SPE-28367: Society of Petroleum Engineers, presented at SPE ACTE, New Orleans, LA.

Kleinberg, R. L. and Boyd A., 1997, Tapered cutoffs for magnetic resonance bound water volume, SPE-38737: Society of Petroleum Engineers, presented at the 1997 Annual Technical Conference and Exhibition.

Lindquist, W. B., Venkatarangan, A., Dundmuir, J., and Wong, T., 2000, Pore and throat size distributions measured from synchrotron X-ray tomographic images of Fontainebleau sandstones: *Journal of Geophysical Research*, vol. 105 (B9), p. 21509–21527.

Peaceman, D. W., and Rachford, H. H., 1955, The numerical solution of parabolic and elliptic differential equations: *Journal of the Society for Industrial and Applied Mathematics*, vol. 3, no. 1, p. 28–41.

Ramakrishnan, T. S., Schwatz, L. M., Fordham, E. J., Kenyon, W. E., and Wilkinson, D. J., 1999, Forward models for nuclear magnetic resonance in carbonate rocks: *The Log Analyst*, vol. 40, no. 4, p. 260–270.

Reid, R. C., Prausnitz, J. M., and Poling, B. E., 1987, *The Properties of Gases and Liquids*: McGraw Hill, New York.

Straley, C., Morriss, C. E., Kenyon, W. E., and Howard, J. J., 1995, NMR in partially saturated rocks: Laboratory insights on free fluid index and comparison with borehole logs: *The Log Analyst*, vol. 36, no. 1, p. 40–56.

Todd, M. R., O’Dell, P. M., and Hirasaki, G. J., 1972, Methods of increased accuracy in numerical reservoir simulators: *SPEJ*, vol. 12, no. 6, p. 515–530.

Toumelin, E., Torres-Verdín, C., Chen, S., and Fischer, D. M., 2003, Reconciling NMR measurements and numerical simulations: Assessment of temperature and diffusive coupling effects on two-phase carbonate samples: *Petrophysics*, vol. 44, no. 2, p. 91–107.

Trantham, J. C. and Clampitt, R. L., 1977, Determination of oil saturation after waterflooding in oil-wet reservoir - The North Burbank Unit, Tract 97 Project: *Journal of Petroleum Technology*, vol. 29, no. 1, p. 491–500.

Zhang, G. Q., Hirasaki, G. J., and House, W. V., 2001, Effect of internal field gradients on NMR measurements: *Petrophysics*, vol. 42, no. 1, p. 37–47.

Zhang, G. Q., Hirasaki, G. J., and House, W. V., 2003, Internal field gradients in porous media: *Petrophysics*, vol. 44, no. 6, p. 422–434.

#### APPENDIX A

The governing equations (3-5) in terms of dimensionless variables (with superscript \*) are

$$\frac{\partial^2 M^*}{\partial x^{*2}} + \frac{\partial^2 M^*}{\partial y^{*2}} = \alpha \frac{\partial M^*}{\partial t^*} \quad (\text{A.1})$$

$$\frac{\partial M^*}{\partial x^*} - \mu S(y^*) M^* = 0 \text{ at } x^* = 0, 0 \leq y^* \leq 1 \quad (\text{A.2})$$

$$\frac{\partial M^*}{\partial x^*} = 0 \text{ at } x^* = \eta^{-1}, 0 \leq y^* \leq 1 \quad (\text{A.3})$$

$$\frac{\partial M^*}{\partial y^*} = 0 \text{ at } y^* = 0 \text{ and } 1, 0 \leq x^* \leq \eta^{-1}. \quad (\text{A.4})$$

In the above system, the discontinuous boundary condition along the  $y$ -axis is combined into a single equation by using the step function  $S(y^*)$  defined as

$$\begin{aligned} S(y^*) &= 1 \text{ for } 0 \leq y^* \leq \beta \\ &= 0 \text{ for } \beta < y^* \leq 1 \end{aligned} \quad (\text{A.5})$$

#### APPENDIX B

##### Numerical solution

The non-dimensionalized equations (A.1-A.5) are numerically integrated for the time evolution of magnetization in the pore. However, the direct numerical integration leads to non-physical oscillations in the solution due to round off errors. Instead, the governing equations are expressed in residual form by expressing the unknown as the change in magnetization from the previous iteration as shown

$$\delta M^{k+1} = M^{k+1} - M^k \quad (\text{B.1})$$

where  $k$  refers to the iteration index. The equations are then solved for the change in magnetization at each iteration step and the solution added to magnetization at previous step to yield the magnetization at the current step. The iterations are continued till the residual falls below the error tolerance. An Alternating-Direction-Implicit finite difference technique (Peaceman and Rachford, 1955) is employed for the numerical integration. A sequence of four iteration parameters 0.75, 0.075, 0.0075, 0.00025 is found to be optimal in reducing the number of iterations per time step. The time truncation errors are controlled by using an automatic time step ( $\Delta t$ ) selector algorithm (Todd et al., 1972).  $\Delta t$  at the next time step is scaled by the ratio of maximum change in  $M$  desired to maximum change in  $M$  over the entire domain at the previous time step. Thus, the time truncation errors are limited due to small  $\Delta t$  in the beginning of the simulation (when the rate of change of  $M$  is large) and large  $\Delta t$  towards the end.

The decay curve is obtained by summing the magnetization values over the entire domain at each time step. Simulated decay data are sampled at the times corresponding to

0.5% change in the average magnetization and fitted to a multi-exponential distribution to obtain the  $T_2$  distribution

$$\overline{M(t_i)} \approx \sum_j f_j \exp(-t_i / T_{2,j}) \quad (\text{B.2})$$

where  $\overline{M(t_i)}$  is the average magnetization in the entire domain at discrete times ( $t_i$ ). The coefficients  $f_j$  are obtained by minimizing the following objective function (Dunn et al., 1994)

$$\sum_i \left[ \overline{M(t_i)} - \sum_j f_j \exp(-t_i / T_{2,j}) \right]^2 + \lambda \sum_j f_j^2. \quad (\text{B.3})$$

In the above expression,  $\lambda$  is the regularization parameter. The numerical scheme is validated by comparing the numerical solution with the analytical solution obtained by Brownstein and Tarr (1979) for the case of  $\beta = 1$  for different values of  $\mu$ . In all cases, the two solutions match within an accuracy of 0.1% (maximum relative error) indicating the correctness of the numerical solution.

### APPENDIX C

We resolve the issue of faster relaxation of micropore in the coupled case than in the decoupled case, observed in our simulations. For the case of no diffusional coupling, the dimensionless relaxation time of the micropore is inversely proportional to its surface-to-volume ratio i.e.

$$\lim_{\alpha \rightarrow \infty} T_{2,\mu} = \lim_{\alpha \rightarrow \infty} \frac{T_{2,\mu}}{T_{2,c}} = \frac{L_1 / \rho}{L_1 / \rho \beta} = \beta. \quad (\text{C.1})$$

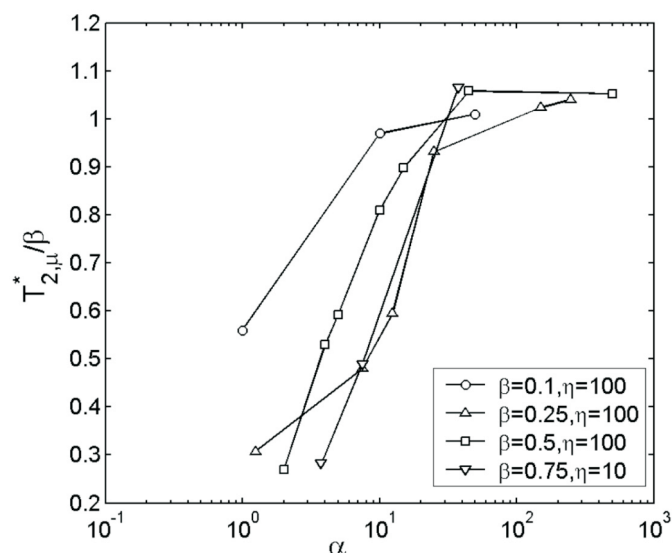


**FIG. C.1** Plot of micropore relaxation time with  $\alpha$  for different simulation parameters. Micropore appears to relax faster when coupled with macropore.

Hence, when coupling between micro and macropore is allowed, the micropore is expected to relax slower than  $\beta$ . Figure C.1 shows the normalized relaxation time of micropore peak as a function of  $\alpha$  for different simulation parameters. We see that for the decoupled regime, the normalized micropore relaxation time tends to 1 as expected. But for the intermediate coupling regime, it appears that the micropore is relaxing faster than the decoupled rate i.e.  $T_{2,\mu}^* < \beta$ . This artifact of faster relaxation of micropore in the coupled case was also observed in Ramakrishnan's analysis (1999). No explanation was, however, offered in their paper.

The apparent contradiction is resolved by studying the early relaxation data of the coupled pore. Analysis of the initial slope of the decay curve reveals that the system relaxes with a unit relaxation time. This is because at very short times, the fluid in micro and macropore does not have sufficient time to exchange by diffusion with each other. Thus, the micropore decays with relaxation time of  $\beta$  while macropore relaxes with infinite relaxation time.

$$\begin{aligned} M^* &= \beta \exp(-t / \beta) + (1 - \beta) \exp(-t / \infty) \\ &\approx \beta(1 - t / \beta) + (1 - \beta) \quad (t < < 1) \quad (\text{C.2}) \\ &= 1 - t \approx \exp(-t). \end{aligned}$$

However, at longer times, macropore relaxes with a finite relaxation time due to diffusional coupling with the micropore. This decrease in relaxation time of the macropore has an apparent effect of reducing the relaxation time of the micropore. Figure C.2 shows the simulated

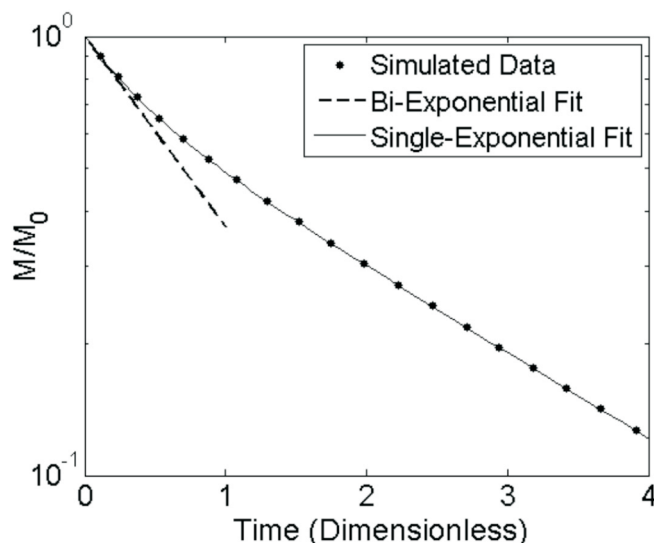


**FIG. C.2** Simulated relaxation data for  $\alpha = 10$  ( $\beta = 0.5$ ,  $\eta = 100$  and  $\mu = 0.2$ ). The black dashed line is an exponential decay with relaxation time of 1. The solid line is a bi-exponential fit ( $0.26 \exp(-t/0.4) + 0.74 \exp(-t/2.2)$ ) of the data.

relaxation data for the case of  $\beta = 0.5$ ,  $\eta = 100$  and  $\mu = 0.2$  ( $\alpha = 10$ , intermediate coupling regime). The system initially decays with unit relaxation time as shown by the dashed line. However, a bi-exponential fit (solid line) to the data estimates the relaxation time of the micropore to be 0.4 which is less than the expected value of 0.5. The inconsistency arises due to decrease in relaxation time of the macropore from infinity at short times to 2.2 at longer times.

#### ABOUT THE AUTHORS

**Vivek Anand** is working as a tool physicist with Schlumberger Oil Field Services in Sugar Land, Texas, USA. Vivek obtained his Bachelor of Technology in Chemical Engineering from Indian Institute of Technology in 2002 and a PhD from Rice University in 2007, also in Chemical Engineering. His research focuses on restricted diffusion, diffusional coupling and internal gradients in NMR well logging.

**George J. Hirasaki** obtained a BS from Lamar University in 1963 and a PhD from Rice University in 1967, both in Chemical Engineering. George had a 26-year career with Shell Development and Shell Oil Companies before joining the Chemical Engineering faculty at Rice University in 1993. At Rice, his research areas are in NMR well logging, reservoir wettability, enhanced oil recovery, gas hydrate recovery, asphaltene deposition, emulsion coalescence and surfactant foam aquifer remediation. He received the SPE Lester Uren Award in 1989. He was named an Improved Oil Recovery Pioneer at the 1998 SPE/DOR IOR Symposium. He was the 1999 recipient of the Society of Core Analysts Technical Achievement Award. He is a member of the National Academy of Engineers.